Nanoscale

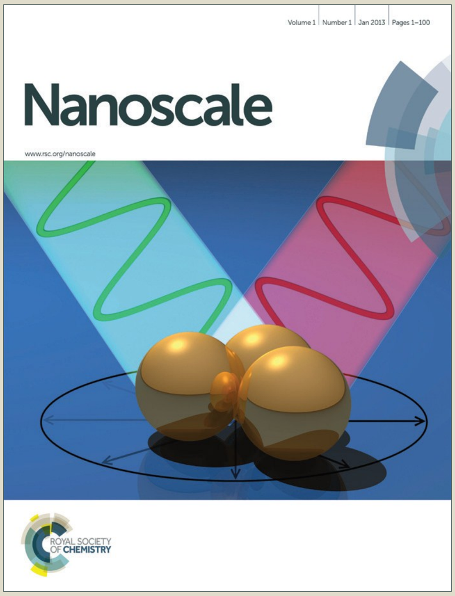

ROYAL SOCIETY OF CHEMISTRY

www.rsc.org/nanoscale

Journal Name

ARTICLE

Multiple coupling in plasmonic metal/dielectric hollow nanocavity arrays for high sensitive detection†

Received 00th January 20xx,
Accepted 00th January 20xx

DOI: 10.1039/x0xx00000x

www.rsc.org/

Jun Yin,[a] Yashu Zang,[a,b] Chuang Yue,[a,b] Xu He,[a,b] Hongtao Yang,[c] De-Yin Wu,[c] Min Wu,[d] Junyong Kang,[b] Zhihao Wu[e*] and Jing Li[a*]

Recently, plasmonic coupled optical cavity has gained much attention due to its attractive properties in light manipulation, e.g. high Q optical resonance, local field enhancements and extraordinary transmission. The strongly enhanced local field originated from the plasmonic resonance hybridizing with the optical cavity mode presents great potential application in chemical and biological sensing. Here, the multiple coupling effect between plasmonic mode and optical cavity mode has been demonstrated in self-assembled metal/dielectric hollow-nanosphere (HNS) arrays and the strongly enhanced local field originated from the inter-coupling of the plasmonic cavities was further employed for high sensitive recyclable SERS sensing.

Introduction

Surface-enhanced Raman scattering (SERS)[1] is becoming a leading nondestructive technique which can elevate the sensitivity of Raman spectroscopy to a single molecule detection regime by manipulating the surface plasmons.[2, 3] When metal nanostructures interact with the incident light, the electrons coherently oscillating on the surfaces, also known as surface plasmon resonance (SPR) effect,[4] would generate a strong localized near field, which is well acknowledged as the main mechanism for surface plasmon based SERS. In order to achieve the single molecular level detection, 'hot spots', in which strong local surface plasmon resonance (LSPR) effect or its inter-coupling effect generally occur, have been widely investigated and applied in previous works.[5-7] Beside of the SERS applications, the inter-coupling effect between designed plasmonic nanostructures also has been widely used in the SPR based sensitive detection,[8] such as molecular monolayer sensing and ultrahigh refractive index sensing.[9-11]

On the other hand, optical cavities, which fundamentally present the ability for light confinement due to the whispering gallery mode (WGM) or Fabry-Perot resonances in them, have also been proposed for SERS detection by using the highly confined light in the cavity to generate Raman photons.[12, 13] Additionally, when coupling the cavity mode with SPR mode from metal nanostructures near or surrounding them, hybridization resonance modes generally happen and special near-field and far-field optical properties will emerge.[14, 15] This kind of plasmonic coupled optical cavity, also called plasmonic cavity, has gained much attention due to its attractive properties in light manipulation, e.g. high Q optical resonance,[14] local field enhancements[15, 16] and extraordinary transmission.[16, 17] Therefore, it has been widely proposed to be used in enhancing semiconductor emission,[18] plasmonic laser,[14, 19] WGM resonator based bio-sensor,[15] nanosensor with high figure-of-merit[10] and other related fields requiring superior optical performances. Undoubtedly, the well-controlled local near field also exhibits attractive application in high sensitive SERS chips, as demonstrated by Chanda *et al* recently in the quasi-three-dimensional plasmonic crystals.[16] Practically, further employing of inter-coupling effect between these hybrid plasmonic cavities with already achieved strong local field to generate much stronger hot spots would be more attractive on high sensitive SERS detections. However, this kind of multiple coupling in metal/dielectric nanocavity arrays and its application to SERS detection have not been studied in detailed yet.

In this work, plasmonic coupled WGM resonance in self-assembled metal/dielectric double-shell hollow nanospheres (HNSs) was demonstrated and proposed to generate hot spots utilizing the multiple coupling effects between the plasmonic cavities for the application to high sensitive SERS detection. Series orders of plasmonic coupled WGM resonances in Ag/ZnO double-shell HNS arrays were characterized by the transmission spectroscopy and recognized through the resonance spectra and near field patterns by FDTD simulations. Highly localized near field around the HNS cavities originated

---

[a] *Pen-Tung Sah Institute of Micro-Nano Science and Technology, Xiamen University, Xiamen, 361005, China. E-mail: lijing@xmu.edu.cn*
[b] *Department of Physics, Xiamen University, Xiamen, 361005, China.*
[c] *College of Chemistry and Chemical Engineering, Xiamen University, Xiamen, 361005, China.*
[d] *Xiamen Entry-Exit Inspection and Quarantine Bureau, Xiamen, 361026, China.*
[e] *Wuhan National Laboratory for Optoelectronics, School of Optical and Electronic Information, Huazhong University of Science and Technology, Wuhan, 430074, China. E-mail: zhihao.wu@hust.edu.cn*

† Electronic Supplementary Information (ESI) available. See DOI: 10.1039/x0xx00000x

from the plasmonic WGM resonance and its strong multiple coupling effect between the HNS arrays ensure this plasmonic cavity arrays to be a suitable SERS substrate. Extraordinary SERS performances were then achieved on the HNS arrays with optimized size and gaps, and even the analyte rhodamine 6G (R6G) and *para*-Aminothiophenol (PATP) with the concentration down to 10^{-10} M still can be detected. Additionally, more significant photocatalytic self-cleaning process can be effectively accomplished on this recyclable SERS chips under visible light irradiation rather than conventional UV illumination. Further Raman mapping from this metal/dielectric double-shell hollow structure evidences this periodic plasmonic cavity arrays to be a stable and uniform SERS-active substrate. The demonstration of the multiple coupling effects induced by the plasmonic coupled WGM resonances in these size-tunable metal/dielectric nanocavity arrays provides new guidelines to modulate local and far field optical properties within a broadband light range.

Results and discussion

As fabricated Ag/ZnO HNS arrays.

The Ag/ZnO double-shell HNS periodic arrays were fabricated using the self-assembled polystyrene (PS) nanospheres as template combined with the magnetron sputtering technology. The fabrication processes are schematically shown in Figure S1 (Supporting Information, SI) by using the colloidal template method[20] as described in our previous work.[21] Figure 1a shows the as-fabricated ZnO HNS arrays with the detailed information displayed in the inset (i and ii), which clearly demonstrate the hollow and ideal spherical structure except for the contact area with the substrate. Also, smooth surfaces can be visualized in the internal morphology of each optical cavity, which is beneficial for light resonating in the hollow structure. The actual core diameter (*D*) was measured to be ~450 nm when using the 500 nm PS nanospheres as templates followed by RIE etching for 30 seconds and the shell thickness is 45 nm in average. As-produced Ag/ZnO composite HNS arrays fabricated using the PS templates with series RIE etching duration (0, 30, 60 and 90 s) resulting in core diameters of ~480, 450, 420 and 370 nm are shown in the SEM images of Figure 1b-e. It can be seen that the gaps between Ag/ZnO HNSs emerge gradually as the RIE etching time increases and reach a few nanometers employing the etching time of 90 s, which is fundamentally in favor of generating hot spots through the strong inter-coupling effect in the hollow plasmonic cavities.[5]

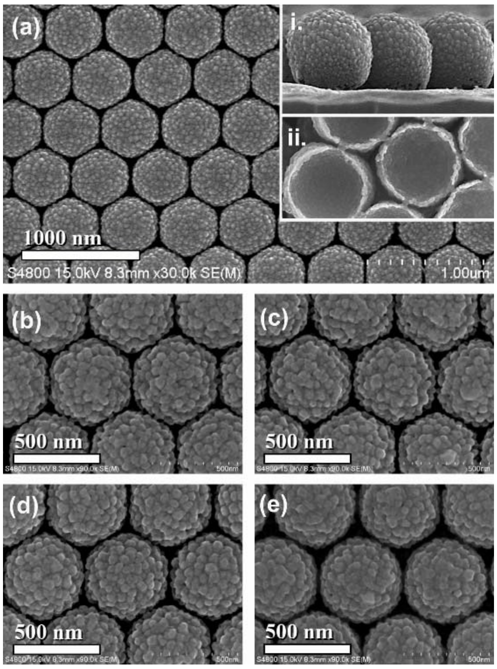

Figure 1. (a) SEM images of as-fabricated ZnO HNS arrays with the insets showing the (i.) cross section of the hollow structure and (ii.) internal morphologies of the inverted ZnO HNSs. (b-e) SEM images of Ag/ZnO HNS arrays adjusted by RIE etching on the PS templates for 0, 30, 60 and 90 s, respectively.

Plasmonic coupled WGM resonances.

In order to verify the resonance properties in the fabricated ZnO hollow nano-cavity arrays, transmission spectra of the ZnO HNSs on sapphire substrate were measured and compared with the FDTD simulation results as shown in Figure 2a. Several distinguished valleys can be resolved at the wavelengths of 420, 465, 550, and 708 nm in the transmission spectrum, which should originate from the WGM resonances in the ZnO hollow nano-cavity and can be attributed to the corresponding serial resonance orders as marked in the figure.[22] Generally, the WGM resonance in the cavity produces a broad angle scattering of the incident light, which is represented as a dip in the transmission spectra near the resonance wavelength.[23, 24] The simulated transmission spectrum (as displayed in the dash line) of ZnO HNS arrays on sapphire substrate agrees well with the experimental one at the corresponding resonance wavelengths except for a little shift in the third order of WGM resonance, which may originate from non-uniformity of the shell thickness in the as-fabricated ZnO HNSs. Full wave FDTD calculations were performed to simulate the resonance spectrum in this ZnO dielectric 3-D nano-cavity as shown in Figure 2b. Different simultaneously excited cavity modes can be resolved in a single ZnO nano-cavity and the resonance peaks (located at 415, 455, 550, and 700 nm) match well with the transmission spectra in Figure 2a. According to the extracted resonance mode patterns (Figure S2, SI) at each resonance wavelength as illustrated in Figure 2b, the corresponding resonance peaks should be classified as the second to fifth order WGM resonance modes. As for the dip at ~1300 nm in the experimental transmission spectra, it should be the first order Mie resonance mode (TM mode) as demonstrated by the local field distribution in Figure S2c-v. Figure 2d (i) and (ii) show the representative typical simulated near-field distribution around/in a single ZnO nano-cavity under plane wave source excitation at the fourth (455 nm) and fifth (415 nm) order resonance wavelengths. Additionally, those resonances are related to the transverse electric (TE) mode whispering gallery resonances, where the polarizations are perpendicular to the

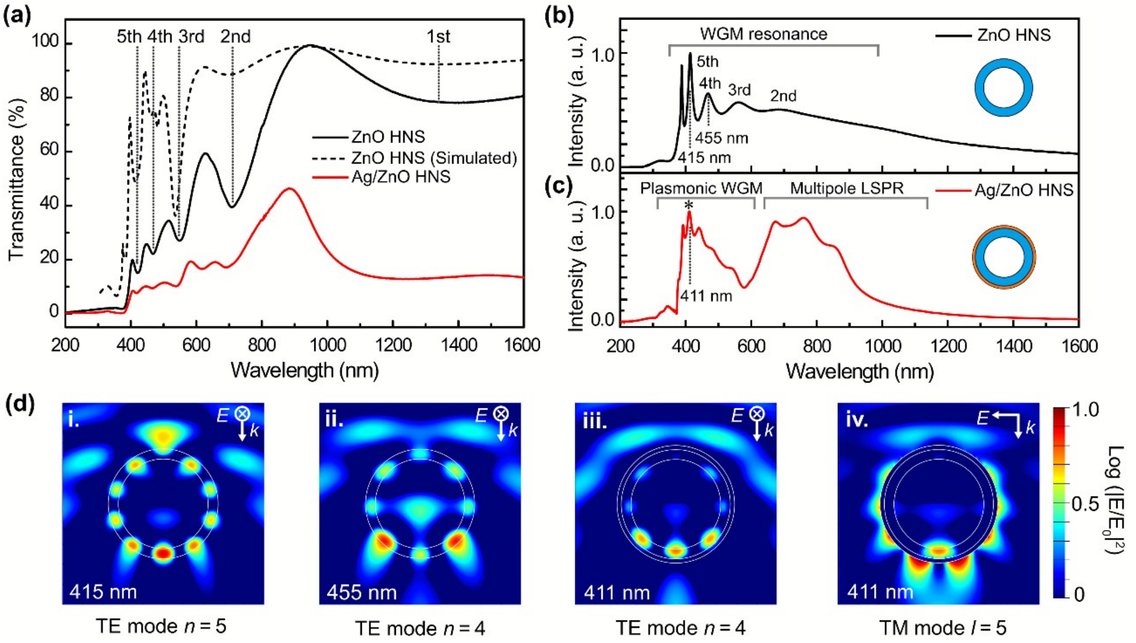

Figure 2. (a) Transmission spectra of the ZnO HNS and Ag/ZnO HNS arrays on sapphire substrates with comparing to the simulated transmission spectrum ZnO HNS arrays. (b) Simulated resonance spectra of a single ZnO HNS nanocavity with the series of TE mode WGM resonances in different orders, and (c) th resonance spectra of a single Ag/ZnO HNS nanocavity with two distinct regions of plasmonic coupled WGM resonance and the only multipole LSP resonanc marked respectively. (d) The extracted typical (i.) fifth and (ii.) fourth order of WGM resonance patterns in the ZnO HNS cavity, and (iii.) TE and (iv.) TM mod like resonance patterns at the resonance peak marked as a star in the resonance spectra of an Ag/ZnO HNS cavity.

cross section of the sphere. Because of the larger reflectivity of the TE-like modes than that of the TM (transverse magnetic)-like (polarization parallel to the cross section of the sphere) modes in the dielectric cavity, the TM-like modes decay faster due to the larger power leakage, especially in such a small cavity.[25] As a result, TE-like mode WGM resonances dominate in this ZnO nanocavity.

After introducing the plasmonic silver shell layer in a thickness of 20 nm outside the ZnO nanocavities, the dips in the corresponding transmission spectra undergo an obvious shift and new dips emerge with an overall reduction of transmission in the whole region, as shown in Figure 2a. The simulated resonance spectra of the Ag/ZnO HNS structure shown in Figure 2c also exhibits the same tendency as the experimental one, which is proposed to come from the coupling of the surface plasmon modes with the dielectric cavity modes. In order to identify the resonance modes in this plasmonic cavity, the simultaneously excited resonance pattern and charges distribution at each resonance wavelength were extracted for further analysis as shown in Figure S3 of SI. According to the extracted near-field and charge distributions at these wavelengths, two distinct regions can be resolved: plasmonic coupled WGM resonance and the regular multipole LSPR regions as illustrated in the figure.

In the plasmonic coupled WGM resonance region, both the TE and TM modes can be well excited and clearly recognized as the series order of WGM cavity resonances (with TE mode dominant) and plasmonic WGM resonances (in TM modes dominance), as summarized in Figure S3b. Undoubtedly, the newly emerged plasmonic WGM resonances should b originated from the hybridization effect between the outer metal shell with the inner ZnO dielectric cavity, which can b explained by the hybridization model[26] as discussed in Figure S4 (SI). The extracted TE and TM mode near-field distributio along the cross section of the spherical Ag/ZnO double shell cavity, related to a specific plasmonic WGM resonance pea marked with a star in Figure 2c, are also selectively shown in Figure 2d (iii) and (iv). For the TE mode as shown in Figure (iii), obviously, the energy is well confined in the inne dielectric hollow cavity due to the larger real part of the Ag's permittivity, which generally causes more field reflected bac to the cavity, leading to a better mode confinement a reported in the previous work.[25] This TE mode resonance a can be identified as the fourth order (n = 4) WGM resonanc according to the eight-lobe resonance pattern. With regard t the TM mode resonance as shown in Figure 2d (iv), obviou plasmonic WGM resonance character can be resolved wit strong localized field generally and intrinsically existing nea the exterior surface of the metal shell and a relatively highe quality (Q) factor.[15] Here, the resonance mode can be wel recognized as the fifth order (l = 5) plasmonic WGM resonanc given the distinguishable ten-lobe pattern and five pairs of positive and negative charge distribution regions aroun exterior surface of the structure (Figure S3b, SI).

While for the multipole LSPR region, located at longe wavelength to the near-infrared, generally no cavity mode could exist in such small cavity since its size is smaller than the incident wavelength. Thus the regular multipole LSPR m resonances dominated this region showing a broadband resonance peak as seen in Figure S3 of SI.

Inter-coupling effect between plasmonic cavities.

It is well acknowledged that the coupling effect of plasmonic structures is strongly dependent on the coupling distance (gaps between the plasmonic cavities within a few nanometers).[5, 27, 28] As shown in Figure 1e, the gaps between ZnO HNS nanocavities can be produced within a few nanometers (<10 nm) by the RIE etching on PS template with the time increased to 90 s, where strong coupling can be expected to occur. As the size of the PS nanosphere decreases with increasing the RIE etching time on the templates, the WGM resonance peaks corresponding to each specific order around the ZnO HNSs and Ag/ZnO HNSs both undergo an apparent blue shift as shown in Figure 3a and b. Meanwhile, with the gaps between the Ag/ZnO HNS arrays emerging gradually, the inter-coupling effect is also enhanced as demonstrated in the near field distributions shown in Figure 3c i-iii, which were simulated using the typical core diameters of 450, 420 and 370 nm consistent with the experimental results. As the core diameter of the Ag/ZnO cavities decreases with longer time RIE etching on the template, stronger local near field can be produced in the gaps. Specifically, the coupling effect in the gaps can induce as high as 10^3 fold electrical intensity enhancement within a 2 nm distance manipulated by reducing the size of the plasmonic cavity, as illustrated in Figure 3c-iv. According to the simulation results, the visually enhanced local field near the surface and gaps originated from the multiple coupling: plasmonic coupled WGM resonance and the inter-coupling effect between the plasmonic nanocavities, evidence that the Ag/ZnO double-shell plasmonic cavity array can be quite promising for applications to high sensitive SERS sensing.

SERS application.

SERS characterizations were firstly performed on the kinds of plasmonic nanocavity arrays with different core diameters using R6G as the target analyte to evaluate the local field enhancement originated from the multiple coupling effects. The results well agree with the FDTD simulation ones as discussed above that high Raman scattering intensity can be obtained on the plasmonic cavities as shown in Figure S5 (SI). The SERS active property of Ag/ZnO HNS plasmonic structure has also been compared with other structures like bare Ag HNS arrays, Ag/ZnO film and bare ZnO HNS substrate, as shown in Figure 4. Metal hollow nanostructure has been demonstrated to have superior advantages for SERS through the enhanced local field due to SPR and the generated hot-spots induced by the coupling effect.[28-30] However, in this work, the plasmonic coupled nanocavity arrays apparently exhibit much better performance on SERS detection by showing a rather stronger Raman enhancement than that in the bare Ag HNS arrays. Owning to the higher loss of only plasmonic modes than the dielectric modes,[25] the dielectric cavity is more suitable for light confinement *via* the WGM resonance than the bare metal cavity structure, thus in this manner the much better SERS performance was accomplished in the Ag/ZnO cavity rather

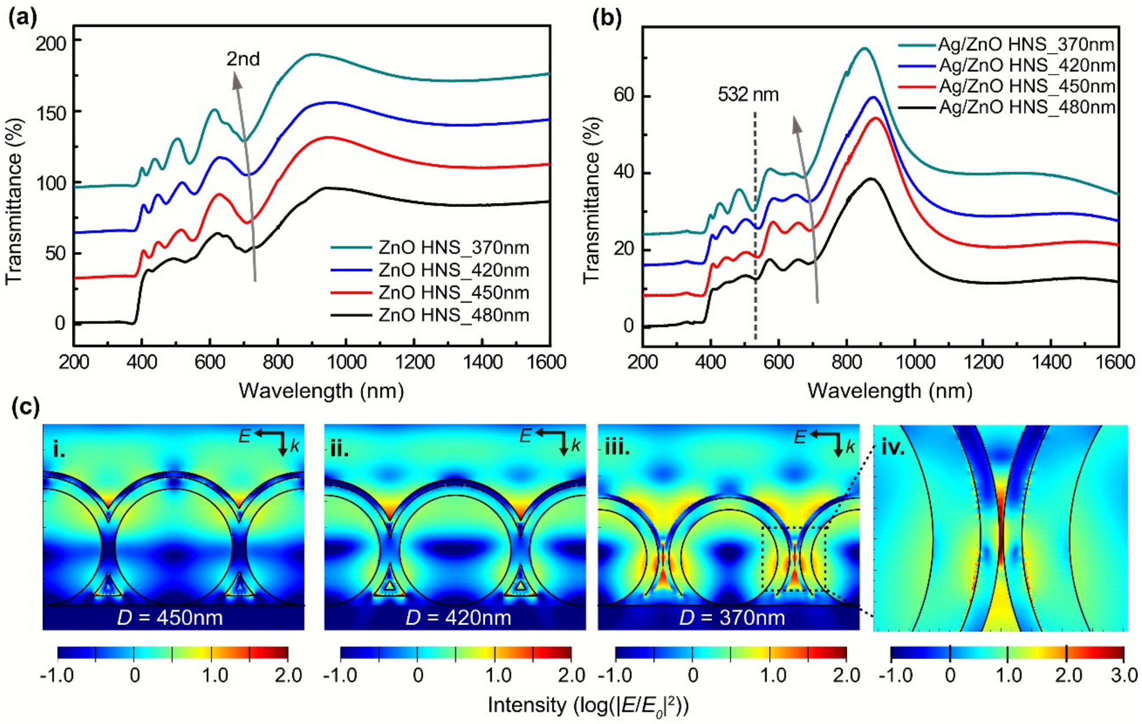

Figure 3. The experimental transmission spectra of as-fabricated (a) ZnO and (b) Ag/ZnO HNS arrays with the core diameters (*D*) of 480, 450, 420 and 370 nm using 500 nm PS nanospheres as the templates treated by RIE with series of etching time of 0, 30, 60 and 90 s, respectively. (c) (i.-iii.) the simulated near field distributions of Ag/ZnO plasmonic nanocavity arrays with three typical core diameters of ~450, 420 and 370 nm consistent with those in (a) and (b); (iv.) The enlarged near-field distribution at the gap of the plasmonic cavities in (iii.).

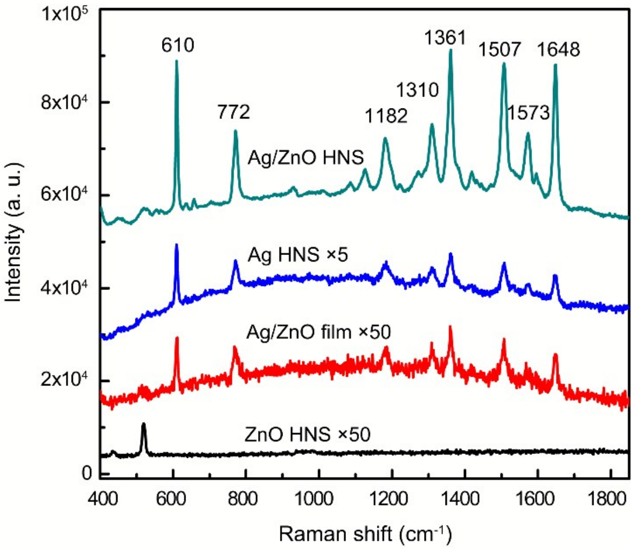

Figure 4. SERS characterization on the Ag/ZnO plasmonic cavity arrays compared with other structures: bare Ag HNS arrays (shell thickness of 40 nm), Ag/ZnO double film and bare ZnO HNS arrays (shell thickness of 45 nm) structures. The characterized Raman bands located at 610, 772, 1182, 1310, 1361, 1507, 1573 and 1648 cm^{-1} marked in the spectra belong to the typical Raman vibrations of R6G and match well with the reported results in the literature.[31]

than in the bare metal hollow arrays. Additionally, even strong local field can be obtained on the bare metal hollow structures through the inter-coupling effect from the higher order LSPR modes, these modes would be suppressed rapidly when a rough surface presents on the metal shell due to the extensive surface topography dependence of the LSPR modes.[32] For Ag/ZnO film sample, due to the lacking of LSP resonance and plasmonic inter-coupling effect, understandably much lower SERS signals was obtained.[21] In the case of the bare ZnO HNS arrays, local electric field on the exterior surface could not be very high due to the absence of SPR property, although effective light confinement can be induced by the WGM resonance in the nanocavities.[22] So, no Raman signals can be resolved when using such low concentration of R6G analyte. Even so, the ZnO HNS arrays still exhibit a better SERS performance compared with the bare silicon substrate when using high concentration of R6G (Figure S6, SI).

In order to evaluate the detecting sensitivity of this plasmonic coupled metal/dielectric SERS substrate, different concentration of the analyte R6G ranging from 10^{-5} to 10^{-10} M and PATP ranging from 10^{-4} to 10^{-10} M were used to perform the Raman measurements on the sample with the core diameter of 370 nm. Figure 5a shows the Raman spectra of R6G on the SERS substrate of plasmonic cavity arrays as function of the probe concentration. Obvious Raman signals of R6G still can be resolved as seen in Figure 5b even with the concentration down to 10^{-10} M. This result evidently demonstrates the high Raman detecting sensitivity, even up to the single molecular level in the detecting area (~10^{-10} -10^{-11} M R6G),[2] can be realized on this plasmonic coupled nanocavity arrays as a SERS substrate. Furthermore, an at least 10^9 Raman enhancement factor (EF) can be achieved by calculating the SERS enhancement ratio compared with Raman signals on the bare ZnO film substrate when using higher concentration of R6G analyte (10^{-2} M). The Raman measurement results of PATP also exhibit the similar sensitivity that the corresponding characteristic Raman signals still can be recognized even at a

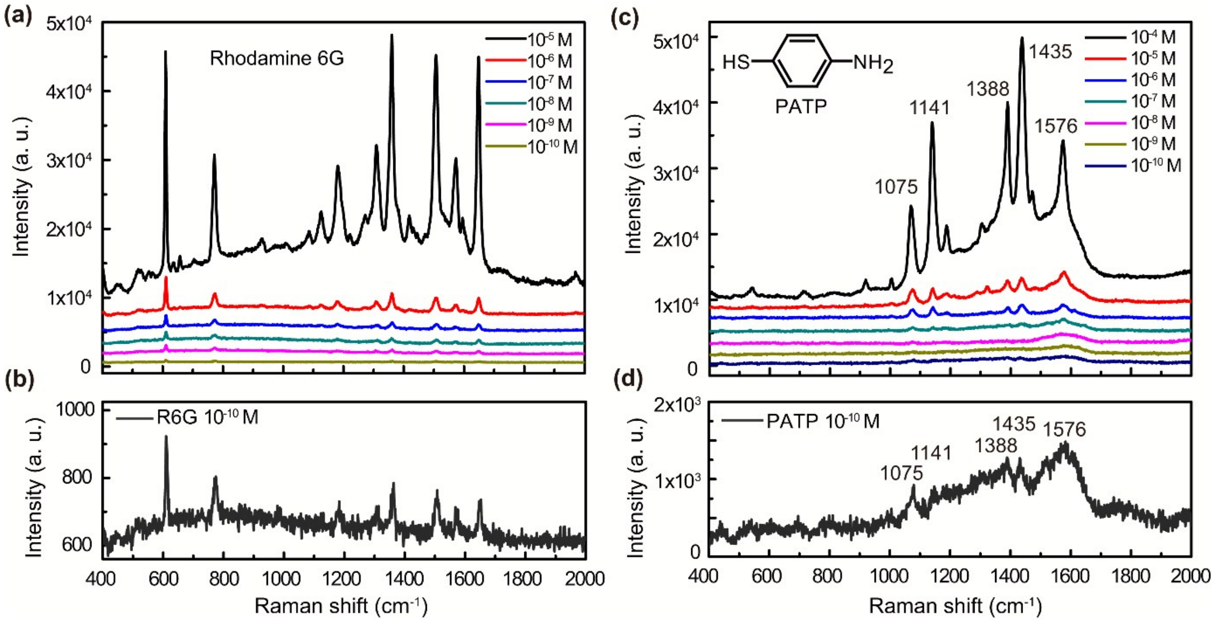

Figure 5. (a) Raman spectra of R6G on the Ag/ZnO HNS arrays as a function of concentration ranging from 10^{-5} M to 10^{-10} M and (b) the representative Raman spectrum of R6G in the concentration of 10^{-10} M; (c) Raman spectra of PATP on the Ag/ZnO HNS arrays as a function of concentration varying from 10^{-4} M to 10^{-10} M and (d) the representative Raman spectrum of PATP in the concentration of 10^{-10} M. The laser power used in the SERS measurement is 0.025 mW for R6G and 5 mW for PATP, respectively.

low concentration of 10^{-10} M as shown in Figure 5c and d. The observed Raman shifts at 1078, 1142, 1389, 1435 and 1577 cm^{-1} demonstrate the typical SERS signals from the species 4, 4'-dimercaptoazobenzene of the PATP coupling reaction according to the previous report,[33, 34] which are different from the PATP solid materials (Figure S7, SI).

By taking advantage of the obtained strong local near-field around the metal/semiconductor composite nanocavity arrays, effective photocatalytic activity assisted by the plasmonic-coupled-optical-cavity modes can be achieved and the obvious self-cleaning process has been realized on the SERS chips by evaluating the Raman signals as shown in Figure 6. Apparently, much more significant photocatalytic degradation performance on R6G probe can be accomplished under visible light irradiation rather than UV illumination, which is quite different from previous works commonly presenting higher photocatalytic efficiencies in UV region on wide-band-gap based nanostructures.[35, 36] Generally, the hot electrons generated by the plasmonic resonance on metal nanostructures are the main reason for the visible light induced photocatalytic,[37-39] as well as the photodegradation effect on R6G probe in this work. Here, the broadband light manipulation induced by the plasmonic coupled WGM resonances and strong local field generated by the multiple coupling effect make the Ag/ZnO plasmonic nanocavity arrays to be efficient for visible light induced photocatalysis, which is quiet meaningful for employment of solar energy. Further detailed study is undergoing in our most recent work.

It is well known that the uniformity is very important for practical application of Raman sensing chips. Then, Raman mapping was performed on the as-fabricated Ag/ZnO HNS double shell arrays as seen in the CCD image of Figure S8a within the marked large scale area of 9 µm × 9 µm, as displayed in Figure S8b. Each pixel in the confocal Raman mapping images represents integral Raman intensity near Raman shift of 1360 cm^{-1} in the interested region (1320 cm^{-1} ~ 1400 cm^{-1}) as shown in (c). The mapping image and the histogram of Raman intensities in Figure S8e evidently demonstrate that uniform SERS signals can be obtained on this self-assembled plasmonic coupled metal/dielectric double shell cavity arrays.

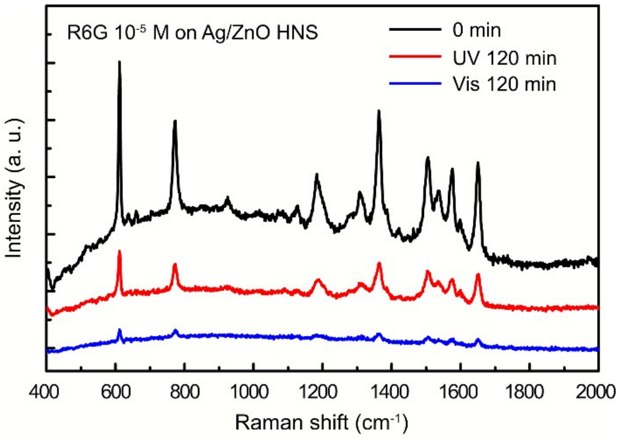

Figure 6. UV and visible light induced photodegradation of R6G adsorbed on the Ag/ZnO HNS arrays evaluated by the Raman spectra for the same irradiation time of 120 min.

Conclusions

In conclusion, multiple coupling effect has been experimentally and theoretically demonstrated in the self-assembled metal/dielectric double-shell hollow nanocavity arrays. The highly localized electric field originated from plasmonic coupled WGM resonances on the surface and consequently generated hot spots due to the inter-coupling between the plasmonic cavities ensure this composite nanostructure array to be a suitable SERS substrate for bio-sensing. In this manner the high sensitive SERS performance with the detectable R6G and PATP probe concentration down to 10^{-10} M and EF up to 10^9 was accomplished on this Ag/ZnO HNS arrays with optimized size and gaps. Besides UV illumination, more significant photodegradation of R6G induced by visible light irradiation can be achieved on this recyclable SERS chip. Further Raman mapping characterization also demonstrate high uniformity on this SERS substrate, which is much meaningful for the practical application of this kind of recyclable SERS chips to bio-sensing, analytical chemistry and so on.

Furthermore, the specific light manipulation property in near field and far field in the metal/dielectric nanocavity arrays make them have other fascinating potential applications: i). By utilizing the strongly enhanced local field near the hollow nanosphere induced by the plasmonic WGM resonance, SPASER (surface plasmon amplification by stimulated emission of radiation) based nanolaser arrays can be potentially realized; ii). Broadband light trapping can be technically and fundamentally proposed by taking advantage of the series of plasmonic WGM and LSP resonances covering from UV to near-infrared region; iii). With the merit of the enhanced strong local field induced by these resonances, multi-wavelength excited SERS chips can be fabricated for studying the mixed analytes when the Raman vibrations from each of them is sensitive to a specific excitation wavelength.

Experimental

Fabrication of Ag/ZnO double-shell HNS periodic arrays. The Ag/ZnO double-shell HNS periodic arrays were fabricated using the self-assembled PS nanospheres as template combined with the magnetron sputtering technology. Commercial PS nanospheres purchased from Thermo Scientific with the diameter of 500 nm were used as template materials to fabricate the double-shell HNS arrays. The fabrication processes are schematically shown in Figure S1 by using the colloidal template method[15] as described in our previous work.[16] In brief, firstly, spin-coating method was employed to self-assemble monolayer PS nanospheres both on silicon and sapphire substrates with a hydrophilic surface. Reactive-ion etching (RIE) for different durations was introduced to adjust the size and distribution of the PS template. Then, ZnO film was deposited on the substrates using magnetron sputtering method followed by a thermal annealing process to form ZnO HNS arrays with an improved crystal quality. Finally, another Ag film depositing process proceeded to produce the double-shell Ag/ZnO hollow structure.

Characterization. The morphologies of the samples were investigated using a Hitachi S-4800 field-emission SEM. Transmission spectra of all the samples on sapphire substrates were carried out by the UV-Vis-NIR spectrophotometer (Varian, UV-Vis-NIR Cary 5000). The SERS properties were characterized by a confocal Raman spectroscopy (Renishaw inVia Raman Microscope) with a 532 nm laser excitation source. The Raman mapping was performed on a confocal Raman imaging system (WITec Confocal Raman Microscope Alpha 300) equipped with a 488 nm laser excitation source. The photocatalytic activities of the samples under UV and visible light irradiation were evaluated by the Raman signals' intensity of R6G on corresponding substrates. During the photocatalytic processes, a 18 W Philips UV lamp emitting line ranging from 340 to 410 nm with a main wavelength at 365 nm and an Xenon lamp (500 W) with a UV light filter (cut-off at the wavelength of 400 nm) in an optical power of 100 mW cm^{-2} were used as the UV and visible light sources, respectively.

Acknowledgements

The authors would like to thank Prof. N. F. Zheng from the Chemistry Department of Xiamen University for constructive discussion and suggestions. This work was financially supported by the MOST of China (2009CB930704), National Natural Science Foundation of China (61106118), the 12th Five Years Key Programs (2012BAK08B01), and Science and Technology Program of Public Wellbeing of Xiamen City of China (3502Z20144079).

Notes and references

‡ Footnotes relating to the main text should appear here. These might include comments relevant to but not central to the matter under discussion, limited experimental and spectral data, and crystallographic data.

1. M. G. Albrecht and J. A. Creighton, *J. Am. Chem. Soc.*, 1977, **99**, 5215-5217.
2. S. Nie and S. R. Emory, *Science*, 1997, **275**, 1102-1106.
3. K. Kneipp, Y. Wang, H. Kneipp, L. T. Perelman, I. Itzkan, R. R. Dasari and M. S. Feld, *Phys. Rev. Lett.*, 1997, **78**, 1667.
4. H. Raether, *Surface plasmons on smooth surfaces*, Springer, 1988.
5. L. Tong, H. Xu and M. Käll, *MRS Bull.*, 2014, **39**, 163-168.
6. S. K. Ghosh and T. Pal, *Chem. Rev.*, 2007, **107**, 4797-4862.
7. L. M. Liz-Marzán, C. J. Murphy and J. Wang, *Chem. Soc. Rev.*, 2014, **43**, 3820-3822.
8. K. M. Mayer and J. H. Hafner, *Chem. Rev.*, 2011, **111**, 3828-3857.
9. M. Koenig, M. Rahmani, L. Zhang, D. Y. Lei, T. R. Roschuk, V. Giannini, C.-W. Qiu, M. Hong, S. Schlücker and S. A. Maier, *ACS nano*, 2014, **8**, 9188-9198.
10. M. A. Schmidt, D. Y. Lei, L. Wondraczek, V. Nazabal and S. A. Maier, *Nature Commun.*, 2012, **3**, 1108.
11. Y. Zhan, D. Y. Lei, X. Li and S. A. Maier, *Nanoscale*, 2014, **6**, 4705-4715.
12. I. Alessandri, *J. Am. Chem. Soc.*, 2013, **135**, 5541-5544.
13. M. S. Anderson, *Appl. Phys. Lett.*, 2010, **97**, 131116-131116-131113.
14. B. Min, E. Ostby, V. Sorger, E. Ulin-Avila, L. Yang, X. Zhang and K. Vahala, *Nature*, 2009, **457**, 455-458.
15. Y.-F. Xiao, C.-L. Zou, B.-B. Li, Y. Li, C.-H. Dong, Z.-F. Han and Q. Gong, *Phys. Rev. Lett.*, 2010, **105**, 153902.
16. D. Chanda, K. Shigeta, T. Truong, E. Lui, A. Mihi, M. Schulmerich, P. V. Braun, R. Bhargava and J. A. Rogers, *Nature Commun.*, 2011, **2**, 479.
17. Y. L. Ho, G. Lerondel and J. J. Delaunay, *IEEE Photonic. Tech. L.*, 2014, **26**, 1979-1982.
18. C.-H. Cho, C. O. Aspetti, J. Park and R. Agarwal, *Nature Photon.*, 2013, **7**, 285-289.
19. M. Stockman, *Nature Phys.*, 2014, **10**, 799-800.
20. F. Caruso, R. A. Caruso and H. Möhwald, *Science*, 1998, 282, 1111-1114.
21. J. Yin, Y. Zang, C. Yue, Z. Wu, S. Wu, J. Li and Z. Wu, *J. Ma Chem.*, 2012, **22**, 7902-7909.
22. J. Yin, Y. Zang, C. Yue, X. He, J. Li, Z. Wu and Y. Fang, *Phys. Chem. Chem. Phys.*, 2013, **15**, 16874-16882.
23. Y. Yao, J. Yao, V. K. Narasimhan, Z. Ruan, C. Xie, S. Fan and Y. Cui, *Nature Commun.*, 2012, **3**, 664.
24. M. López-García, J. Galisteo-López, C. López and A. García-Martín, *Phys. Rev. B*, 2012, **85**, 235145.
25. C.-Y. Ni, S.-W. Chang, D. J. Gargas, M. C. Moore, P. Yang and S. L. Chuang, *IEEE J. Quantum Elect.*, 2011, **47**, 245-251.
26. E. Prodan, C. Radloff, N. J. Halas and P. Nordlander, *Science*, 2003, **302**, 419-422.
27. L. Zhang, H. Chen, J. Wang, Y. F. Li, J. Wang, Y. Sang, S. J. Xiao, L. Zhan and C. Z. Huang, *Small*, 2010, **6**, 2001-2009.
28. M. Mahmoud, B. Snyder and M. El-Sayed, *J. Phys. Chem. C*, 2010, **114**, 7436-7443.
29. R. Li, H. Zhang, Q.-W. Chen, N. Yan and H. Wang, *Analyst*, 2011, **136**, 2527-2532.
30. J. Yin, Y. Zang, B. Xu, S. Li, J. Kang, Y. Fang, Z. Wu and J. Li, *Nanoscale*, 2014, **6**, 3934-3940.
31. H. Watanabe, N. Hayazawa, Y. Inouye and S. Kawata, *J. Phys. Chem. B*, 2005, **109**, 5012-5020.
32. H. Wang, G. P. Goodrich, F. Tam, C. Oubre, P. Nordlander and N. J. Halas, *J. Phys. Chem. B*, 2005, **109**, 11083-11087.
33. Y.-F. Huang, H.-P. Zhu, G.-K. Liu, D.-Y. Wu, B. Ren and Z.-Q. Tian, *J. Am. Chem. Soc.*, 2010, **132**, 9244-9246.
34. D.-Y. Wu, X.-M. Liu, Y.-F. Huang, B. Ren, X. Xu and Z.-Q. Tian, *J. Phys. Chem. C*, 2009, **113**, 18212-18222.
35. X. Li, G. Chen, L. Yang, Z. Jin and J. Liu, *Adv. Funct. Mater.*, 2010, **20**, 2815-2824.
36. G. Sinha, L. E. Depero and I. Alessandri, *ACS Appl Mater. Interfaces*, 2011, **3**, 2557-2563.
37. S. Mubeen, J. Lee, N. Singh, S. Krämer, G. D. Stucky and M. Moskovits, *Nature Nanotechnol.*, 2013, **8**, 247-251.
38. P. Christopher, H. Xin, A. Marimuthu and S. Linic, *Nature Mater.*, 2012, **11**, 1044-1050.
39. Y. Zang, J. Yin, X. He, C. Yue, Z. Wu, J. Li and J. Kang, *J. Mater. Chem. A*, 2014, **2**, 7747-7753.